

High-temperature large-gap quantum anomalous Hall insulator in ultrathin double perovskite films

Santu Baidya^{1,*}, Umesh V. Waghmare², Arun Paramakanti^{3,4}, Tanusri Saha-Dasgupta^{5,†}

¹ *Department of Physics and Center for Nanointegration Duisburg-Essen (CENIDE),*

University of Duisburg-Essen, Lotharstrasse 1, 47057 Duisburg, Germany.

² *Jawaharlal Nehru Centre for Advanced Scientific Research, Jakkur, Bangalore 560064, India.*

³ *Department of Physics, University of Toronto, Toronto, Ontario, Canada M5S 1A7.*

⁴ *Canadian Institute for Advanced Research, Toronto, Ontario, M5G 1Z8, Canada.*

⁵ *Department of Condensed Matter Physics and Materials Science,*

S. N. Bose National Centre for Basic Sciences, Kolkata 700 098, India.

(Dated: August 11, 2016)

Motivated by the goal of realizing topological phases in thin films and heterostructures of correlated oxides, we propose here a quantum anomalous Hall insulator (QAH) in ultrathin films of double perovskites based on mixed $3d$ - $5d$ or $3d$ - $4d$ transition metal ions, grown along $[111]$ direction. Considering the specific case of ultrathin $\text{Ba}_2\text{FeReO}_6$, we present a theoretical analysis of an effective Hamiltonian derived from first-principles. We establish that a strong spin-orbit coupling at Re site, t_{2g} symmetry of the low-energy d -bands, polarity of its $[111]$ orientation of perovskite structure, and mixed $3d$ - $5d$ chemistry results in room temperature magnetism with a robust QAH state of Chern number $C = 1$ and a large band-gap. We uncover and highlight a non-relativistic *orbital Rashba*-type effect in addition to the spin-orbit coupling, that governs this QAH state. Our prediction of a large topological band-gap of ~ 100 meV in electronic structure, and a magnetic transition temperature $T_c \sim 300\text{K}$ estimated by Monte Carlo simulations, is expected to stimulate experimental efforts at synthesis of such films and enable possible practical applications of its dissipationless edge currents.

PACS numbers: 71.20.Be, 71.15.Mb, 71.20.-b

I. INTRODUCTION

Quantum anomalous Hall insulators are two-dimensional (2D) band insulators exhibiting a quantized Hall conductivity^{1,2} in the presence of magnetic order that spontaneously breaks time-reversal symmetry. The requisite intrinsic nonzero Berry curvature³ for such anomalous Hall effect could appear either due to the adiabatic motion of electrons in magnetically ordered backgrounds with nontrivial pinned spin-textures⁴⁻⁸ or from spin-orbit coupling (SOC) even in simple collinear ferromagnetic (FM) or antiferromagnetic states.⁹⁻¹¹

Following a theoretical proposal¹², the first observations of QAHs have been made in topological insulator (TI) thin films doped with magnetic Cr or V atoms, with a FM T_c of ~ 15 – 20 K, and a quantized $\sigma_{xy} = e^2/h$ observed for $T \lesssim 0.5\text{K}$.^{13,14} There have been other proposals for QAHs, yet to be realized, via depositing magnetic atoms on graphene^{15,16} or by putting heavy atoms with large SOC on magnetic substrates.¹⁷ These proposals share a common feature of topologically nontrivial bands derived from s or p orbitals. Given the potential applications of chiral edge currents associated with QAH in dissipationless electronic circuits,² its desirable for practical applications that one would like to i) boost the temperature scale for QAH effect, ii) engineer a large topological band-gap, and iii) avoid possible dopant or adatom-induced inhomogeneity by considering stoichiometric composition.

Considering the recent progress in growing oxide heterostructures along different crystallographic

directions,¹⁸⁻²² and the drive towards integrated oxide electronics,^{23,24} ultrathin films of transition metal oxides (TMOs) appear to be an attractive possibility in the above context. Compared to s or p orbitals based systems, TMOs with d orbital dominated band structure has the possibility of high temperature realization. Seminal theoretical studies^{25,26} on perovskite bilayers grown along the $[111]$ crystallographic direction predicted that the combination of the buckled honeycomb structure and SOC can lead to 2D time-reversal invariant topological insulator in t_{2g} bands in SrIrO_3 and LaOsO_3 bilayers, as well as interaction-induced stabilization of QAHs in flat e_g bands of LaAuO_3 bilayers. Following this, ultrathin films hosting nickelate e_g orbitals²⁶⁻³¹ and pyrochlore iridate $j_{\text{eff}} = 1/2$ orbitals³²⁻³⁴ were proposed to exhibit TIs as well as QAHs with Chern number $C = 1$. However, an important challenge which is faced in most single-TM based QAHs proposed, is the fact that correlations need to be strong enough to drive magnetism and break time-reversal symmetry. At the same time, it should not be so strong so as to cause complete Mott localization.³¹ Recently, the $[001]$ interface between TiO_2 and the half-semimetal CrO_2 has been proposed to form a QAH,³⁵ with higher Chern number $C = 2$, but unfortunately exhibiting a small gap of $\sim 4\text{meV}$.

Taking a step forward, a promising class of materials is that of naturally occurring bi-component TM perovskite compounds with ordered structure, i.e. the double perovskite (DP) compounds of general composition $\text{A}_2\text{BB}'\text{O}_6$ with rock-salt ordering of two different TM atoms, B and B'³⁶. For example, in a $3d$ - $5d$ or $3d$ - $4d$ DP, the $3d$ TM atoms (B) can allow for a high energy

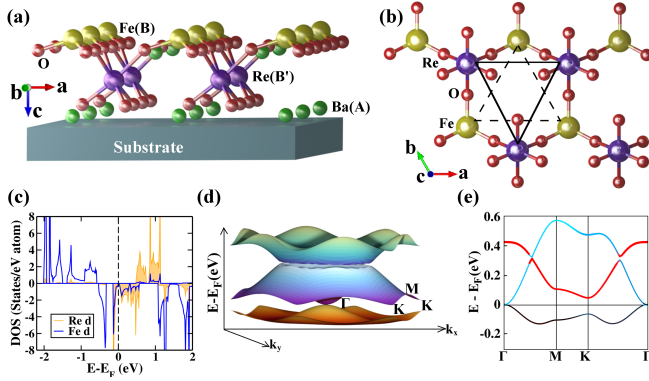


FIG. 1: (Color online) (a): Bilayer of $\text{Ba}_2\text{FeReO}_6$ (BFRO), with c-axis pointed along the $[111]$ growth direction and terminated at Fe layer. (b): Buckled honeycomb network of Re and Fe atoms, viewed along the growth direction. Ba, Re, Fe and O atoms have been marked. In (b) Ba atoms have been omitted for clarity. (c): Spin-polarized GGA density of states projected onto Fe and Re d states. (d): The GGA band structure in minority spin channel plotted in the hexagonal BZ. (e): Same as in (d), but plotted along high symmetry directions; the colors (cyan/light gray, black, red/dark gray) show dominant orbital characters (d_{xy} , $d_{x^2-y^2}$, $d_{3z^2-r^2}$).

scale for magnetism, while the $5d$ or $4d$ TM atoms (B') can feature strong SOC, making them ideal candidates in search for high temperature QAHs. Physical separation of the ions which host magnetism from the ions which host strong SOC, as in the DPs, avoids the issue related to interplay of correlation effect and SOC at the same site, as in the case of single TM based candidates. Furthermore, in many of these $3d$ - $5d$ or $3d$ - $4d$ DP materials, the low-energy physics are typically described by t_{2g} -orbital bands of $5d$ TM ions, which together with strong oxygen-covalency can strongly suppress the Jahn-Teller (JT) distortion. This is in contrast to e_g -orbital based proposals which are prone to strong JT distortions that tend to favor trivial insulators.^{37,38}

In this article, we consider the case of $\text{Ba}_2\text{FeReO}_6$ (BFRO), which in bulk, is a half-metallic FM with high T_c of $\approx 305\text{K}$.³⁹ Here, the Ba, Fe and Re atoms occupy the A, B and B' sites respectively. Using first-principles density functional theory (DFT) calculations, combined with effective model calculations we show that an ultrathin $[111]$ film of BFRO, consisting of layers of Fe/BaO₃/Re/BaO₃, forms a $C = 1$ QAH insulator with a large topological gap $\sim 100\text{meV}$ and an estimated FM $T_c \sim 315\text{K}$. The large-gap and high T_c should enable practical use of our proposal.

It is worth mentioning that our work goes well beyond earlier studies of DP films.^{40,41} In particular our study identifies three key ingredients for formation of this QAH, which should be broadly applicable to other t_{2g} physics dominated $3d$ - $5d$ or $3d$ - $4d$ half-metallic DPs like $\text{Sr}_2\text{FeMoO}_6$, Sr_2CrWO_6 with strong ferromagnetism^{42,43} driven by the $3d$ ion:

- (1) Ultrathin films of such half-metallic oxides grown along the $[111]$ direction show a strong trigonal distortion, favoring a non-Kramers doublet formed from $5d$ or $4d$ TM ion derived t_{2g} orbitals in reduced C_3 crystal field symmetry. Following this, the band structure of the conducting spin channel features symmetry-protected linear Dirac band touchings at the hexagonal Brillouin zone (BZ) corners ($\pm K$) and a single quadratic band touching (QBT) at the Γ -point.
- (2) The breaking of in-plane inversion symmetries by localized $3d$ TM ions gaps out the Dirac points at the BZ corners. The source of the gap opening at the Dirac points is traced to a non-relativistic *orbital Rashba*-type effect. For appropriate filling of the $5d/4d$ ion, this leads to a half-semimetal, with the Fermi energy E_F pinned to the QBT point.
- (3) The strong SOC of $5d/4d$ TM ion gaps out the QBT. For a filling where E_F was pinned to the QBT point, this leads to a QAH with a topological gap. The strong SOC and the trigonal distortion also combine to pin the $5d/4d$ TM moments to be perpendicular to the plane, leading to a high FM T_c .

II. DFT CALCULATIONS

Fig.1 shows the structure of an ultrathin $[111]$ bilayer film of BFRO. The $[111]$ growth direction results in the stacking of BaO₃, Re, BaO₃, Fe layers. The bilayer is terminated at the Fe layer facing vacuum, the bottom BaO₃ layer being supported by the substrate, as shown in Fig.1(a).⁴⁴ This results in three-fold oxygen coordination of Fe atom and six-fold oxygen coordination of Re atom, forming a buckled honeycomb lattice with two interpenetrating triangular lattices of Fe and Re atoms, as shown in Fig.1(b). The atomic positions in the constructed thin film geometry were completely relaxed within the DFT optimization scheme, while the in-plane lattice constant of the film was held fixed at a_0 , with $a_0 = 5.6922\text{\AA}$ being the lattice constant for bulk BFRO, which is in almost perfect commensuration with the substrate of the cubic BaTiO₃.⁴⁵ The buckled honeycomb lattice geometry for the $[111]$ growth direction introduces a trigonal distortion in ReO₆ octahedra, signaled by $\approx 3.7^\circ$ deviation of O-Re-O bond angles from 90° . The DFT calculations employed for structural optimization as well as for self-consistent calculation of electronic structure were carried out within the generalized gradient approximation (GGA)⁴⁶ for the exchange-correlation functional. We checked that our results were qualitatively unchanged upon incorporating correlation effects within GGA+U.⁴⁷ We used two choices of basis sets: (i) the plane-wave based pseudopotential method as implemented in the Vienna An-initio Simulation Package (VASP)⁴⁸ and (ii) the full potential linear augmented plane-wave method of Wien2k.⁴⁹ GGA calculations were also carried out including SO for the

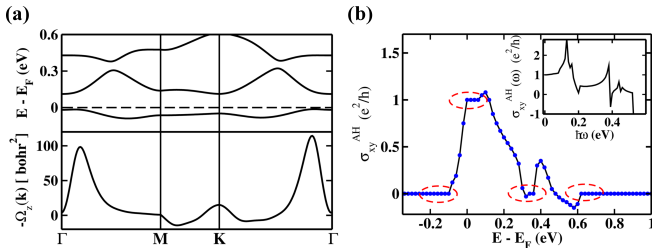


FIG. 2: (Color online) (a): GGA+SO band structure in minority spin channel (top panel) and calculated Berry curvature (bottom panel) plotted along the high symmetry directions in the BZ. (b): Anomalous Hall conductivity of the band structure in (a), in units of e^2/h . Quantized plateaus are highlighted. Inset: Frequency dependence of the real part of the optical AH conductivity $\sigma_{xy}^{AH}(\omega)$ in units of e^2/h .

Re $5d$ states, which is a crucial ingredient to drive the QAHI. For details of DFT calculations, see Appendix A.

Fig.1(c) shows the GGA spin-polarized DOS (without SO), projected onto Fe d and Re d states. The GGA results in a completely gapped solution in the majority spin channel, while a semimetallic state is obtained in the minority spin channel. Our first important observation is that while the Fe d states are completely occupied in the majority spin channel as in case of bulk DOS,⁴¹ in contrast to bulk DOS we also find occupancy of Fe d states in the minority spin channel, apart from the presence of strongly hybridized Fe-Re states close to E_F . This suggests that Fe in the thin film geometry of BFRO to be in a nominal d^6 or $2+$ state, as opposed to the nominal d^5 or $3+$ oxidation state in bulk BFRO, the latter being established by x-ray magnetic circular dichroism (XMCD) experiment³⁹ and by DFT calculations.^{41,50} Considering the nominal $2+$ and $2-$ valences of Ba and O, this puts Re in a d^1 or $6+$ valence state. This observation is validated by the computed magnetic moments of $2.99 \mu_B$ ($-0.39 \mu_B$) at Fe (Re) site as compared to bulk values of $3.73 \mu_B$ ($-0.78 \mu_B$).⁴¹ Nevertheless, the net moment in the cell is identical to the bulk value of $3.0 \mu_B$, with a significant fraction of the moment residing at oxygen sites in both cases due to the strong covalency effect. Thus, remarkably, the reduction of dimensionality in moving from bulk to ultrathin films, resulting in reduced O-coordination at Fe site, causes strong redistribution of charges between Fe and Re. As discussed below, this is one of the crucial aspect in defining the low energy electronic structure and the resulting QAHI.

We next focus on the details of the low energy minority spin band structure in the 2D Brillouin zone (BZ). This is found to consist of three sheets as shown in Fig.1(d), dominantly consisting of the three t_{2g} orbitals of Re, admixed with O p and Fe t_{2g} characters. The three-fold O-coordination on the Fe sites, leads to a highly reduced C_3 symmetry, as opposed to the bulk octahedral symmetry. This imprints itself as a strong trigonal distortion in the low energy band structure, splitting the Re t_{2g} states into doubly degenerate e_g^π and singly degenerate

a_{1g} state, with a_{1g} state being energetically higher than e_g^π , as defined in the local octahedral coordinate system. In terms of global coordinates of the cell, they correspond to linear combinations of $d_{xy}/d_{x^2-y^2}$, and $d_{3z^2-r^2}$.

We find isolated gapped bands everywhere in the BZ, except at the Γ point, where the valence and conduction bands touch quadratically [cf Fig. 1(d)]. Orbital projection of the band structure, as presented in Fig.1(e), shows that out of the three bands, the a_{1g} ($d_{3z^2-r^2}$) band remains completely empty. The other two bands exhibit a QBT at Γ , one of them being fully occupied and another being empty, in order to satisfy the nominal d^1 filling of Re. Thus the $[111]$ thin film geometry of BFRO with d^1 filling of Re, gives rise to a *half semi-metallic* band structure.

Starting with this GGA result, we next turn on the SOC. This induces an orbital moment of $0.13 \mu_B$ at Re site, pointing opposite to the spin moment. As shown in Fig. 2(a), the most dramatic effect of SOC on the band structure is at the Γ point, where it splits the QBT, opening up a gap of ≈ 100 meV and triggering a completely insulating state. Using WANNIER90,⁵¹ which employs an interpolation scheme, we have computed the Berry curvature $\Omega_z(\mathbf{k})$ over a fine \mathbf{k} -mesh in the BZ. Fig.2(b) plots $\Omega_z(\mathbf{k})$ along high symmetry directions, showing that it is concentrated close to the Γ -point. The anomalous Hall conductivity (AHC) obtained by integrating the Berry curvature over occupied bands in the entire 2D BZ is plotted in Fig.2(b) as a function of varying energy. The nontriviality in band structure shows up as quantized plateaus in this plot (circled for clarity). We have confirmed this result using the Kubo-Greenwood formula⁵² to obtain the anti-symmetric optical conductivity $\sigma_{xy}^{AH}(\omega)$, shown in the inset of Fig. 2(b), with the AHC being given by the real part of $\sigma_{xy}^{AH}(\omega \rightarrow 0)$. These calculations reveal that the insulating state of the $[111]$ thin film of BFRO is a $C = 1$ Chern insulator with a large gap ≈ 100 meV.

We have also computed the effective Fe-Fe magnetic exchange by total energy calculation of different magnetic configurations of Fe spins. For bulk BFRO, our results yield $J_{\text{Fe-Fe}}^{\text{bulk}} \approx 1$ meV, in excellent agreement with inelastic neutron scattering experiments⁵³ (see Appendix B). For the $[111]$ bilayer, we find a larger $J_{\text{Fe-Fe}}^{\text{film}} \approx 3.5$ meV. Using this value, we have carried out classical Monte Carlo simulations of an appropriate spin model of Heisenberg-Ising type. As discussed in Appendix B, we estimate the thin film FM ordering temperature T_c to be ≈ 315 K, which is even slightly higher than the bulk T_c .

III. EFFECTIVE MODEL

In order to gain microscopic understanding, we carry out further analysis in terms of a tight-binding effective model for the three minority-spin bands close to E_F . We work with eigenstates of L_z^{eff} , labeled as $|m_\ell^{\text{eff}}\rangle$, which diagonalize the trigonal crystal field Hamiltonian,

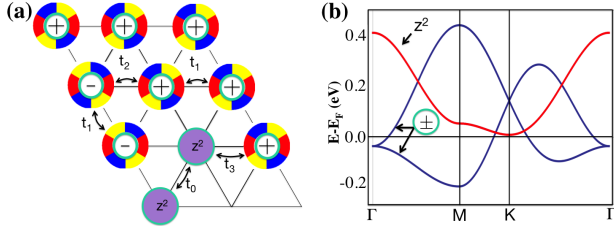


FIG. 3: (Color online) **(a)** The intraorbital (t_0, t_1) and interorbital (t_2, t_3) hoppings on the triangular Re lattice between t_{2g} orbitals with angular momenta $m_\ell = 0$ (denoted z^2) and $m_\ell = \pm 1$. For $m_\ell = \pm 1$, the wheels depict opposite phase windings. **(b)** Decoupled $m_\ell = 0$ and coupled $m_\ell = \pm 1$ bands for $(\Delta_{\text{trg}}, t_0, t_1, t_2) = (60, 45, 20, 80)$ meV, where all other terms in Hamiltonian have been set to zero (see text).

\hat{z} being the [111] direction. In global coordinates, $|0\rangle \equiv |d_{3z^2-r^2}\rangle$ is at higher energy, while $|\pm 1\rangle \equiv \frac{1}{\sqrt{2}}(|d_{x^2-y^2}\rangle \pm i|d_{xy}\rangle)$ form a low energy non-Kramers doublet (see Appendix C). The $|m_\ell^{\text{eff}}\rangle$ orbitals are schematically shown in Fig.3(a), with $z^2 \equiv |0\rangle$ depicted as filled circles and the $|\pm 1\rangle$ orbitals having opposite phase windings of $\mp 2\pi$ corresponding to the appropriate real space wavefunctions, shown by color wheels in the figure. We set $\Psi_{\mathbf{k}}^\dagger = (c_{\mathbf{k}\uparrow 0}^\dagger, c_{\mathbf{k}\uparrow +}^\dagger, c_{\mathbf{k}\uparrow -}^\dagger)$ in the m_ℓ -basis, and consider $H_{\text{eff}} = \sum_{\mathbf{k}} \Psi_{\mathbf{k}}^\dagger H_{\mathbf{k}} \Psi_{\mathbf{k}}$. The intraorbital $[\varepsilon(\mathbf{k})]$ and interorbital $[\eta(\mathbf{k})]$ dispersions in $H_{\mathbf{k}}$ are given by,

$$\varepsilon_0(\mathbf{k}) = -2t_0(\cos k_1 + \cos k_2 + \cos k_3)$$

$$\varepsilon_{\pm}(\mathbf{k}) = -2t_1(\cos k_1 + \cos k_2 + \cos k_3) - \Delta_{\text{trg}} \pm \gamma_{\mathbf{k}}^R \mp \frac{\lambda}{2}$$

$$\eta_{+-}(\mathbf{k}) = 2t_2(\cos k_1 + \omega \cos k_2 + \omega^2 \cos k_3)$$

$$\eta_{0+}(\mathbf{k}) = \eta_{0-}^*(\mathbf{k}) = 2t_3(\cos k_1 + \omega \cos k_2 + \omega^2 \cos k_3),$$

where $k_1 = k_x$, $k_2 = -k_x/2 + k_y\sqrt{3}/2$, $k_3 = -k_1 - k_2$, and $\omega = \exp(i2\pi/3)$. Here we have set t_0, t_1 are intraorbital hopping amplitudes, while the interorbital $t_{2,3}$ are complex hoppings due to the phase winding of the $|\pm 1\rangle$ wavefunctions, as shown in Fig. 3(a). Δ_{trg} represents the trigonal splitting. Due to the spin polarized character of these bands, SOC acts as a Zeeman field on the orbital pseudospins via $-\lambda L_z^{\text{eff}} S_z$, λ being the strength of the SOC. Finally, $\gamma_{\mathbf{k}}^R = 2t_R(\sin k_1 + \sin k_2 + \sin k_3)$ encodes an *orbital Rashba*-type effect due to the presence of Fe atoms which break inversion symmetry of the Re lattice, as discussed below.

To clarify the effect of various terms in the effective Hamiltonian, we plot the band structure setting $t_R = \lambda = t_3 = 0$ and fixing $(\Delta_{\text{trg}}, t_0, t_1, t_2) = (60, 45, 20, 80)$ meV. As seen from Fig. 3(b), this broadly reproduces the GGA bandwidth. In this limit, the $|0\rangle$ band is completely decoupled, while the coupled $|\pm 1\rangle$ bands exhibit a C_3 and \mathcal{T} symmetry protected QBT at Γ as well as inversion \mathcal{I} and \mathcal{T} symmetry protected linear Dirac band crossings at $\pm K$, \mathcal{T} being the time-reversal for spinless fermions (as appropriate for a spin-polarized half-metal).

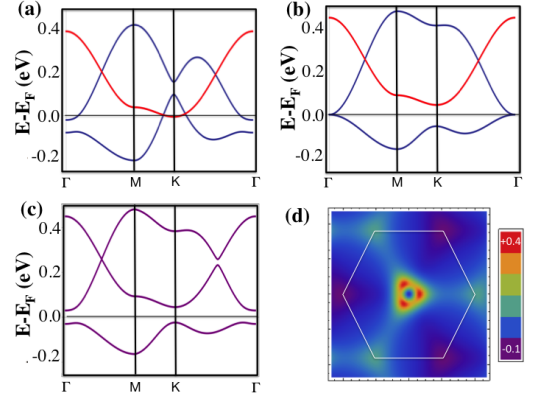


FIG. 4: (Color online) Band structure obtained by setting **(a)** ($t_R = 0, \lambda \neq 0$), **(b)** ($t_R \neq 0, \lambda = 0$), and **(c)** ($t_R \neq 0, \lambda \neq 0$) in the effective Hamiltonian (see text). **(d)** Berry curvature $\Omega_z(\mathbf{k})/2\pi$ for the lowest band, with parameters as in (c), in units where the Re triangular lattice constant is set to unity. The Berry curvature is peaked slightly away from the Γ point, and is asymmetric under $\mathbf{k} \rightarrow -\mathbf{k}$ due to broken inversion.

Turning on SOC, $\lambda \neq 0$, breaks \mathcal{T} and gaps out these band touchings, as illustrated in Fig.4(a) for $\lambda = 30$ meV. The resulting bands derived from $|\pm 1\rangle$ are topologically nontrivial, with Chern numbers $C = \pm 1$; however, the strong dispersion leads to a metal and not a QAHL.

On the other hand, setting $t_R \neq 0$ only breaks \mathcal{I} . As shown in Fig. 4(b) for $t_R = 45$ meV, this only gaps out the Dirac points at $\pm K$, but preserves the QBT at Γ point, perfectly reproducing the GGA dispersion [cf.

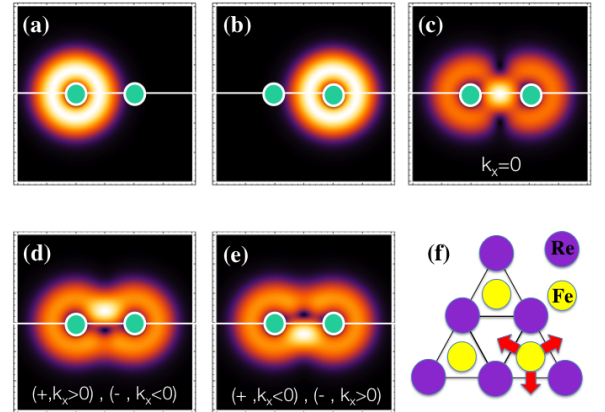


FIG. 5: (Color online) **(a,b)** Electron density for localized pseudospin states $m_\ell = \pm 1$ shown at neighboring Re sites \mathbf{r} and $\mathbf{r} + \hat{x}$. **(c-e)** Bond electronic density obtained by superposing electron density of the same orbital type (both $m_\ell = +1$ or both $m_\ell = -1$) for $k_x = 0$, and $k_x \neq 0$, illustrating electric dipole $\mathcal{P}_y \sim m_\ell^{\text{eff}} \sin k_x$, which changes sign under reversing sign of m_ℓ^{eff} or k_x . **(f)** Triangular lattice structure of Re atoms and underlying Fe atoms. Arrows schematically indicate the in-plane electric fields, generated by symmetry-breaking due to Fe atoms, which can linearly couple to \vec{P} .

Fig.1(e)]. To understand the physical origin of t_R , we plot in Fig. 5(a,b) the ring-like probability density for the $|\pm 1\rangle$ states localized on a pair of neighboring Re sites, positioned at \mathbf{r} and $\mathbf{r} + \hat{x}$, where \hat{x} is a Re triangular lattice bond direction. Remarkably, superposing these two localized states with a relative phase factor of e^{ik_x} , to form a Bloch state at momentum k_x , leads to a probability density distribution which features a \mathbf{k} -dependent bond electric dipole moment $\mathcal{P}_y \sim m_\ell^{\text{eff}} \sin k_x$. This ‘Bloch dipole’ \mathcal{P}_y vanishes for $k_x = 0$ (see Fig. 5(c)), and changes sign under reversing the direction of \mathbf{k} or changing m_ℓ^{eff} from $+1$ to -1 (or vice versa), as shown in Figs. 5(d,e). On the triangular Re lattice, this leads to a \mathbf{k} -dependent ‘Bloch dipole’ which can linearly couple to the electric fields arising due to the presence of Fe atoms breaking the inversion symmetries of the triangular Re lattice, as schematically shown by arrows in Fig.5(f). This gives rise to the term $\gamma_{\mathbf{k}}^R$ in the effective Hamiltonian, as shown in Appendix D. A closely related effect has been shown to account for the spin-orbital texture of surface bands in other materials,^{54,55} though unlike those cases, here the effect arises from in-plane inversion breaking.

Finally, with $t_R \neq 0$ and $\lambda \neq 0$, we are led to a QAHI, with the lowest band having $C = 1$ [cf Fig.4(c)], in agreement with the DFT results. The Berry curvature of the lowest band $\Omega_z(\mathbf{k})$, shown in Fig. 4(d), is concentrated around the Γ -point and is in semi-quantitative agreement with the DFT results. The inversion symmetry breaking is reflected in $\Omega_z(\mathbf{k}) \neq \Omega_z(-\mathbf{k})$.

IV. CONCLUSIONS

Using a combination of first-principles calculations and analysis of an effective Hamiltonian, we have addressed the challenge of possible material realization with a large band-gap, high-temperature Quantum Anomalous Hall insulating state. We propose that ultra-thin films of mixed row ($3d$ - $5d$ or $3d$ - $4d$) double perovskites with $[111]$ orientation have (a) $3d$ TM ions providing strong magnetism, (b) $5d$ or $4d$ TM ions with partially filled t_{2g} bands with a SOC, which make them strong contender for the realization of QAHI. We note that several of these DPs are rare examples of materials with half-metallic ground state with above room temperature Curie temperature, justifying this choice.^{39,42,43} We have demonstrated this for $\text{Ba}_2\text{FeReO}_6$ through rigorous first-principles DFT calculations, corroborated with analysis of a model Hamiltonian. We show that ultrathin $[111]$ film of BFRO is indeed a robust high temperature ($T_c \approx 315\text{K}$), large gap ($\approx 110\text{ meV}$), $C = 1$ QAHI, opening up the possibility of room temperature applications in dissipationless electronic circuit. Edge interfaces of such oxide QAHI states with correlated superconductors might lead to high temperature realization of chiral Majorana edge states.⁵⁹ We have uncovered the key role of the orbital Rashba-type effect, which works hand-in-hand with SOC to drive the nontrivial QAHI. This orbital Rashba-type

effect is expected to play an important role in a broader class of phenomena in orbitally degenerate oxides.

V. ACKNOWLEDGEMENT

S.B. and T.S.D thank Department of Science and Technology, India for the computational facility through Thematic Unit of Excellence of Nano-mission. AP thanks A. M. Cook for preliminary discussions and related collaboration, and acknowledges funding from NSERC of Canada, and support from the Aspen Center for Physics through National Science Foundation grant PHY-1066293. UVW acknowledges support from a Thematic Unit for Computational Materials Science at JN-CASR, and a JC Bose National Fellowship of the department of science and technology, government of India.

Appendix A: Details of DFT Methodology

Our first-principles based density functional theory (DFT) calculations were carried out in the generalized gradient approximation (PBE-GGA)^{46,56,57} of the exchange-correlation potential with a $13 \times 13 \times 2$ k-point grid. The computations were performed in two different ways : (i) using the all-electron full-potential linear augmented plane-wave (FP-LAPW) method as implemented in the WIEN2k code,⁴⁹ and (ii) using a plane-wave-based pseudopotential method as implemented in the Vienna *ab initio* Simulation Package (VASP).⁴⁸ Close results were obtained from two different approaches. The spin-orbit coupling was included in the fully-relativistic schemes.

The muffin-tin radii (R_{MT}), used in FP-LAPW calculations, were 2.50, 1.80, 1.86 and 1.60 a.u. for Ba, Fe, Re and O, respectively. To achieve reasonable accuracy for ground state in the FP-LAPW calculation, the number of plane waves was set by the criteria, $K_{max} \cdot R_{MT} = 7$ where K_{max} is the plane wave cut off value and R_{MT} is the smallest muffin-tin radius. The energy cutoff 600 eV was chosen for calculations in plane wave basis set. The self-consistent convergence was tested with choices of different k-point grids. The ionic position relaxation was carried out in both FP-LAPW and plane wave calculations. For structural optimization a force convergence of $0.01\text{ eV}/\text{\AA}$ was ensured in plane wave basis calculations. On the other hand in FP-LAPW calculations, optimization of the atomic positions were performed using force convergence of 0.001 Ry.a.u^{-1} .

The non-trivial properties were calculated by constructing maximally-localized Wannier functions (MLWFs) for the selected three bands close to Fermi level possessing Re t_{2g} Bloch orbitals character (confirmed from orbital character plotting) using WANNIER90 code⁵⁸ interfaced with WIEN2k code. Starting from DFT generated ground state eigenvalue, eigenstate and Hamiltonian matrices, WANNIER90 is capable of constructing MLWFs corresponding to selected energy

bands.⁵¹ The Berry curvature matrix was calculated for whole Brillouin Zone in the basis of MLWFs. The details of wannierization scheme is available in reference⁶⁰. The intrinsic Anomalous Hall Conductivity was calculated by integrating Berry curvature over dense k mesh of $370 \times 370 \times 65$ on whole Brillouin zone (BZ) using WANNIER90 code. Convergence of AHC value was checked for different choices of dense k-mesh over whole BZ. Further the calculations of ac anomalous Hall conductivity was carried out using Kubo-Greenwood formula for optical conductivity using WANNIER90 code. It gives ac optical conductivity which has both symmetric and anti-symmetric part. The anti-symmetric part gives ac anomalous Hall conductivity which for zero optical frequency gives intrinsic anomalous Hall conductivity (AHC). The details of calculating ac optical conductivity can be obtained in WANNIER90 code⁵⁸.

Appendix B: Finite temperature ferromagnetic transition of thin film: Monte Carlo study

1. Bulk exchange

The DFT calculation of total energy using various Fe magnetic configurations shows that the effective ferromagnetic exchange between Fe moments in bulk BFRO is $J_{FF} = 0.97$ meV. Considering an effective model of only Fe spins (integrating out the Re electrons), this implies that flipping a single spin in the ferromagnetic state leads to an energy cost $E_{\text{flip}} = 2J_{FF}S_F^2z_{\text{fcc}}$ where $z_{\text{fcc}} = 12$ is the coordination number on the fcc lattice of Fe moments and S_F is the effective Fe spin. Alternatively the magnetic exchange can be computed from a spin model where both Fe and Re are retained in the model. Within such a picture, the effective description of the magnetism is a Heisenberg model on the Re-Fe lattice, with an antiferromagnetic exchange coupling J_{FR} , which describes ferrimagnetic order with unequal Fe and Re moments. Within such a model, the energy cost to flipping a spin is $E_{\text{flip}} = 2J_{FR}S_F S_R z_c$ where the cubic lattice coordination number $z_c = 6$ and S_R denotes the effective Re spin. Equating the two expressions, we find $J_{FF} = J_{FR}(S_R/S_F)(z_c/z_{\text{fcc}})$. Using $J_{FR} \approx 3$ meV and $S_F/S_R \approx 1.6$ from inelastic neutron scattering experiments⁵³ on bulk BFRO, we find $J_{FF} \approx 0.94$ meV, remarkably close to the DFT estimate.

2. Thin film model

In the thin film geometry, our DFT computation yields $J_{FF} \approx 3.5$ meV, larger than the bulk value. Proceeding as in bulk case, this means flipping a single Fe spin in the ferromagnetic state costs an energy $E_{\text{flip}} = 2J_{FF}S_F^2z_{\Delta}$, where $S_F = 2$ and the triangular lattice coordination number $z_{\Delta} = 6$. Considering the alternative Fe-Re model, we note here, unlike in bulk, the strong trigonal splitting

and large SOC conspire to pin the Re moments to lie perpendicular to the film as discussed in the paper, so they effectively behave as Ising moments $\sigma = \pm 1$. The effective model takes the form

$$H_{\text{Fe-Re}} = J_{FR} \sum_{i \in \text{Fe}, \delta} S_i^z \sigma_{i+\delta} \quad (\text{B1})$$

Note that the Fe spins are still vector spins, only the exchange is highly anisotropic. In the ferrimagnetically ordered state, flipping an Fe spin now costs energy $E_{\text{flip}} = 2J_{FR}S_F|\sigma|z_H$, where $|\sigma| = 1$ and $z_H = 3$ is the honeycomb lattice coordination number. Equating the two expressions, $J_{FR} = S_F J_{FF} z_{\Delta} / z_H \approx 14$ meV. We have carried out Monte Carlo simulations of this mixed Heisenberg-Ising model on the honeycomb lattice. Fig. 6 shows the specific heat divergence [panel (a)] of this model at the paramagnetic to ferromagnetic transition and the order parameter [panel (b)] for a system size of $2L^2$ spins. We have plotted the scaled magnetization $(\frac{m(T)}{m(0)})^8$ corresponding to an Ising exponent $\beta = 1/8$ to illustrate its linear behavior near T_c and data collapse for various system sizes. From such simulations, we estimate $T_c/S_F J_{FR} \approx 0.975(5)$, which yields $T_c \approx 315$ K, which we quote in the paper. Use of a quantum renormalized spin value $S_F^2 \rightarrow S_F(S_F + 1)$ would suggest an even higher estimate for T_c . We have also carried out a simulation of an effective triangular lattice model of vector Fe moments coupled via Ising-exchange interactions (mediated by pinned Re moments), finding very similar results. Our result for the high FM T_c of the thin film is thus robust.

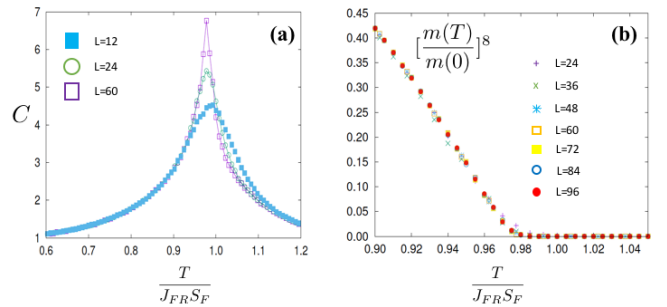


FIG. 6: (Color online) Temperature dependence of (a) specific heat per unit cell of the honeycomb lattice (in units of k_B), and (b) magnetization per site of the honeycomb lattice (normalized to its value at $T = 0$), for the Heisenberg-Ising model in Eq. 1, for illustrative system sizes containing $2L^2$ spins. We have plotted $[m(T)/m(0)]^{1/\beta}$ to illustrate data collapse for an Ising order parameter exponent $\beta = 1/8$. Using these simulations we determine the FM transition temperature $T_c/S_F J_{FR} \approx 0.975(5)$.

Appendix C: Orbital wavefunctions

In the frame of the local octahedral coordinates (x', y', z') , we can express the t_{2g} wavefunctions in terms of angular momentum eigenstates split by the local trigonal distortion as

$$|a_{1g}\rangle = \frac{1}{\sqrt{3}}(|y'z'\rangle + |z'x'\rangle + |x'y'\rangle) \quad (C1)$$

$$|e_{1g}^+\rangle = \frac{1}{\sqrt{3}}(\omega^2|y'z'\rangle + \omega|z'x'\rangle + |x'y'\rangle) \quad (C2)$$

$$|e_{1g}^-\rangle = \frac{1}{\sqrt{3}}(\omega|y'z'\rangle + \omega^2|z'x'\rangle + |x'y'\rangle) \quad (C3)$$

where, $\omega = \exp(i2\pi/3)$. Here, $|a_{1g}\rangle$ refers to the singlet state with $\vec{L}_{\text{eff}} \cdot \hat{n}_{111} = 0$, while e_{1g}^\pm have $\vec{L}_{\text{eff}} \cdot \hat{n}_{111} = \pm 1$. In the text, we work with global coordinates (x, y, z) such that on the Re sites,

$$x' = -\sqrt{\frac{2}{3}}y + \frac{1}{\sqrt{3}}z \quad (C4)$$

$$y' = \frac{1}{\sqrt{2}}x + \frac{1}{\sqrt{6}}y + \frac{1}{\sqrt{3}}z \quad (C5)$$

$$z' = -\frac{1}{\sqrt{2}}x + \frac{1}{\sqrt{6}}y + \frac{1}{\sqrt{3}}z \quad (C6)$$

In these global coordinates, the

$$|a_{1g}\rangle = 3z^2 - r^2 \quad (C7)$$

$$|e_{1g}^\pm\rangle \propto |x^2 - y^2\rangle \pm i|xy\rangle - \frac{1}{\sqrt{2}}(|yz\rangle \pm i|zx\rangle) \quad (C8)$$

Projecting to the $z = 0$ plane of the triangular lattice, the last term does not play an important role, and we thus arrive at the e_{1g} doublet being dominantly given by $d_{x^2-y^2} \pm id_{xy}$, having angular momentum projection perpendicular to the bilayer given by $L_{\text{eff}}^z = \pm 1$.

Appendix D: Orbital Rashba-type effect

1. 1D dispersion

As discussed in the main text of the paper, formation of a Bloch state with momentum \mathbf{k} out of the $m_\ell^{\text{eff}} = \pm 1$ states results into a nonzero electric dipole moment. For one-dimensional motion, for example along \hat{x} , this leads to $\mathcal{P}_y = \alpha m_\ell^{\text{eff}} \sin k$, where α is a proportionality constant and $k \equiv k_x$. If inversion symmetry is broken in the system, such that there is an electric field $\mathcal{E}_y \neq 0$, this leads to an energy correction $-\mathcal{P}_y \mathcal{E}_y$ in the Hamiltonian which shifts the energy of the Bloch state, with the energy shift changing sign for $m_\ell^{\text{eff}} \rightarrow -m_\ell^{\text{eff}}$ or reversing the direction of \mathbf{k} , so that time-reversal is preserved. This can be captured with the Hamiltonian

$$H_R = -i \frac{t_R}{2} \sum_{r,m=\pm 1} m(c_{r,m}^\dagger c_{r+x,m} - c_{r+x,m}^\dagger c_{r,m}) \quad (D1)$$

where r is the site index. In momentum space representation this becomes,

$$H_R = 2t_R \sum_{k,m=\pm 1} \text{sgn}(m) \sin k c_{k,m}^\dagger c_{k,m}, \quad (D2)$$

where $t_R = \alpha \mathcal{E}_y$.

2. 2D triangular lattice

Moving from 1D to the 2D triangular lattice, which is the relevant lattice in this study, each bond on the triangular lattice has a nonzero electric dipole generated by the Bloch state with momentum \mathbf{k} . Now, the set of Fe atoms generates a nonzero electric field perpendicular to the bonds of the Re triangular lattice as depicted in Fig. 5(f) of the paper. In this case, for each bond direction, one gets a coupling of the type discussed in the context of 1D dispersion, leading to the Hamiltonian

$$H = -i \frac{t_R}{2} \sum_{\mathbf{r},m=\pm 2,\delta} m(c_{\mathbf{r},m}^\dagger c_{\mathbf{r}+\delta,m} - c_{\mathbf{r}+\delta,m}^\dagger c_{\mathbf{r},m}) \quad (D3)$$

where $\delta = \hat{x}, -\hat{x}/2 + \sqrt{3}\hat{y}/2, -\hat{x}/2 - \sqrt{3}\hat{y}/2$ denote the three directions on the triangular lattice. In momentum space representation, this yields the term discussed in the paper,

$$H = \sum_{\mathbf{k},m=\pm 2,\delta} \text{sgn}(m) \gamma_{\mathbf{k}}^R c_{\mathbf{k},m}^\dagger c_{\mathbf{k},m} \quad (D4)$$

where $\gamma_{\mathbf{k}}^R = 2t_R(\sin k_1 + \sin k_2 + \sin k_3)$, with $k_1 = k_x$, $k_2 = -k_x/2 + k_y\sqrt{3}/2$, $k_3 = -k_1 - k_2$. Since this is like a Rashba interaction, but with orbital degrees of freedom instead of spin, and with the electric field pointing in the plane rather than out of the plane, we refer to it as an *orbital Rashba*-type effect. The full Hamiltonian must also allow for electric fields pointing out to the plane, which would allow for additional orbital Rashba terms^{54,55} which would drive a conventional Rashba effect in the presence of SOC. A comparison of model calculations with our DFT results however show that the effect of such Rashba terms are small.

* Presently at Center for Correlated Electron Systems, Institute for Basic Science (IBS), Seoul 151-742, Republic

of Korea; Department of Physics and Astronomy, Seoul National University (SNU), Seoul, 151-742, Republic of

Korea.

† Email: t.sahadasgupta@gmail.com

- ¹ F. D. M. Haldane, Phys. Rev. Lett. **61**, 2015 (1988).
- ² C.-X. Liu, S.-C. Zhang, and X.-L. Qi, ArXiv e-prints (2015), 1508.07106.
- ³ D. J. Thouless, M. Kohmoto, M. P. Nightingale, and M. den Nijs, Phys. Rev. Lett. **49**, 405 (1982).
- ⁴ I. Martin and C. D. Batista, Phys. Rev. Lett. **101**, 156402 (2008).
- ⁵ J. W. F. Venderbos, M. Daghofer, J. van den Brink, and S. Kumar, Phys. Rev. Lett. **109**, 166405 (2012).
- ⁶ Y. Akagi, M. Udagawa, and Y. Motome, Phys. Rev. Lett. **108**, 096401 (2012).
- ⁷ Y. Shiomi, M. Mochizuki, Y. Kaneko, and Y. Tokura, Phys. Rev. Lett. **108**, 056601 (2012).
- ⁸ H. Chen, Q. Niu, and A. H. MacDonald, Phys. Rev. Lett. **112**, 017205 (2014).
- ⁹ M. Onoda and N. Nagaosa, Phys. Rev. Lett. **90**, 206601 (2003).
- ¹⁰ C.-X. Liu, X.-L. Qi, X. Dai, Z. Fang, and S.-C. Zhang, Phys. Rev. Lett. **101**, 146802 (2008).
- ¹¹ Z. Qiao, W. Ren, H. Chen, L. Bellaiche, Z. Zhang, A. H. MacDonald, and Q. Niu, Phys. Rev. Lett. **112**, 116404 (2014).
- ¹² R. Yu, W. Zhang, H.-J. Zhang, S.-C. Zhang, X. Dai, and Z. Fang, Science **329**, 61 (2010), ISSN 0036-8075.
- ¹³ C.-Z. Chang, J. Zhang, X. Feng, J. Shen, Z. Zhang, M. Guo, K. Li, Y. Ou, P. Wei, L.-L. Wang, et al., Science **340**, 167 (2013), ISSN 0036-8075.
- ¹⁴ C.-Z. Chang, W. Zhao, D. Y. Kim, H. Zhang, B. A. Assaf, D. Heiman, S.-C. Zhang, C. Liu, M. H. W. Chan, and J. S. Moodera, Nat Mater **14**, 473 (2015).
- ¹⁵ Z. Qiao, S. A. Yang, W. Feng, W.-K. Tse, J. Ding, Y. Yao, J. Wang, and Q. Niu, Phys. Rev. B **82**, 161414 (2010).
- ¹⁶ H. Zhang, C. Lazo, S. Blügel, S. Heinze, and Y. Mokrousov, Phys. Rev. Lett. **108**, 056802 (2012).
- ¹⁷ K. F. Garrity and D. Vanderbilt, Phys. Rev. Lett. **110**, 116802 (2013).
- ¹⁸ B. Gray, H. N. Lee, J. Liu, J. Chakhalian, and J. W. Freeland, Applied Physics Letters **97**, 013155 (2010).
- ¹⁹ M. Gibert, P. Zubko, R. Scherwitzl, J. Íñiguez, and J.-M. Triscone, Nat Mater **11**, 195 (2012).
- ²⁰ S. Catalano, M. Gibert, V. Bisogni, F. He, R. Sutarto, M. Viret, P. Zubko, R. Scherwitzl, G. A. Sawatzky, T. Schmitt, et al., APL Mater. **3**, 062506 (2015).
- ²¹ D. Hirai, J. Matsuno, and H. Takagi, APL Mater. **3**, 041508 (2015).
- ²² S. Middey, D. Meyers, D. Doennig, M. Kareev, X. Liu, Y. Cao, Z. Yang, J. Shi, L. Gu, P. J. Ryan, et al., Phys. Rev. Lett. **116**, 056801 (2016).
- ²³ H. Y. Hwang, Y. Iwasa, M. Kawasaki, B. Keimer, N. Nagaosa, and Y. Tokura, Nat Mater **11**, 103 (2012).
- ²⁴ D. G. Schlom, APL Mater. **3**, 062403 (2015).
- ²⁵ D. Xiao, W. Zhu, Y. Ran, N. Nagaosa, and S. Okamoto, Nat Commun **2**, 596 (2011).
- ²⁶ K.-Y. Yang, W. Zhu, D. Xiao, S. Okamoto, Z. Wang, and Y. Ran, Phys. Rev. B **84**, 201104 (2011).
- ²⁷ A. Rüegg and G. A. Fiete, Phys. Rev. B **84**, 201103 (2011).
- ²⁸ A. Rüegg, C. Mitra, A. A. Demkov, and G. A. Fiete, Phys. Rev. B **85**, 245131 (2012).
- ²⁹ A. Rüegg, C. Mitra, A. A. Demkov, and G. A. Fiete, Phys. Rev. B **88**, 115146 (2013).
- ³⁰ S. Okamoto, Phys. Rev. Lett. **110**, 066403 (2013).
- ³¹ S. Okamoto, W. Zhu, Y. Nomura, R. Arita, D. Xiao, and N. Nagaosa, Phys. Rev. B **89**, 195121 (2014).
- ³² X. Hu, A. Rüegg, and G. A. Fiete, Phys. Rev. B **86**, 235141 (2012).
- ³³ M. Kargarian and G. A. Fiete, Phys. Rev. Lett. **110**, 156403 (2013).
- ³⁴ Q. Chen, H.-H. Hung, X. Hu, and G. A. Fiete, Phys. Rev. B **92**, 085145 (2015).
- ³⁵ T. Cai, X. Li, F. Wang, S. Ju, J. Feng, and C.-D. Gong, Nano Letters **15**, 6434 (2015).
- ³⁶ T. Saha-Dasgupta, Journal of Physics: Condensed Matter **26**, 193201 (2014).
- ³⁷ D. Doennig, S. Baidya, W. E. Pickett, and R. Pentcheva, Phys. Rev. B **93**, 165145 (2016).
- ³⁸ Hongbin Zhang, Huaqing Huang, Kristjan Haule, and David Vanderbilt Phys. Rev. B **90**, 165143 (2014).
- ³⁹ C. Azimonte, J. C. Cezar, E. Granado, Q. Huang, J. W. Lynn, J. C. P. Campoy, J. Gopalakrishnan, and K. Ramesha, Phys. Rev. Lett. **98**, 017204 (2007).
- ⁴⁰ A. M. Cook and A. Paramekanti, Phys. Rev. Lett. **113**, 077203 (2014).
- ⁴¹ S. Baidya, U. V. Waghmare, A. Paramekanti, and T. Saha-Dasgupta, Phys. Rev. B **92**, 161106 (2015).
- ⁴² K. I. Kobayashi, T. Kimura, H. Sawada, K. Terakura, and Y. Tokura, Nature **395**, 677 (1998).
- ⁴³ J. B. Philipp, P. Majewski, L. Alff, A. Erb, R. Gross, T. Graf, M. S. Brandt, J. Simon, T. Walther, W. Mader, et al., Phys. Rev. B **68**, 144431 (2003).
- ⁴⁴ We have also checked the termination of the vacuum facing layer to be Re layer instead of Fe layer. However, this was found to be energetically unfavorable by several eV.
- ⁴⁵ J. J. Wang, F. Y. Meng, X. Q. Ma, M. X. Xu, and L. Q. Chen, Journal of Applied Physics **108**, 034107 (2010).
- ⁴⁶ J. P. Perdew, K. Burke, and M. Ernzerhof, Phys. Rev. Lett. **77**, 3865 (1996).
- ⁴⁷ A. I. Liechtenstein, V. I. Anisimov, and J. Zaanen, Phys. Rev. B **52**, R5467 (1995).
- ⁴⁸ G. Kresse and J. Furthmüller, Phys. Rev. B **54**, 11169 (1996).
- ⁴⁹ S. Blaha, K. Schwartz, G. K. H. Madsen, D. Kvasnicka, and J. Luitz, *WIEN2K, An Augmented Plane Wave + Local Orbitals Program for Calculating Crystal Properties*, Edited by K. Schwarz, Technische Universitaet Wien, Austria (2001).
- ⁵⁰ H. Wu, Phys. Rev. B **64**, 125126 (2001).
- ⁵¹ J. Kunes, R. Arita, P. Wissgott, A. Toschi, H. Ikeda, and K. Held, Computer Physics Communications **181**, 1888 (2010), ISSN 0010-4655.
- ⁵² R. Kubo, Journal of the Physical Society of Japan **12**, 570 (1957).
- ⁵³ K. W. Plumb, A. M. Cook, J. P. Clancy, A. I. Kolesnikov, B. C. Jeon, T. W. Noh, A. Paramekanti, and Y.-J. Kim, Phys. Rev. B **87**, 184412 (2013).

- ⁵⁴ S. R. Park, C. H. Kim, J. Yu, J. H. Han, and C. Kim, Phys. Rev. Lett. **107**, 156803 (2011).
- ⁵⁵ P. Kim, K. T. Kang, G. Go, and J. H. Han, Phys. Rev. B **90**, 205423 (2014).
- ⁵⁶ P. E. Blöchl, Phys. Rev. B **50**, 17953 (1994).
- ⁵⁷ G. Kresse and D. Joubert, Phys. Rev. B **59**, 1758 (1999).
- ⁵⁸ A. A. Mostofi, J. R. Yates, G. Pizzi, Y.-S. Lee, I. Souza, D. Vanderbilt, and N. Marzari, Computer Physics Communications **185**, 2309 (2014), ISSN 0010-4655.
- ⁵⁹ Q. L. He, L. Pan, A. L. Stern, E. Burks, X. Che, G. Yin, J. Wang, B. Lian, Q. Zhou, E. S. Choi, et al., ArXiv e-prints (2016), 1606.05712.
- ⁶⁰ X. Wang, J. R. Yates, I. Souza, and D. Vanderbilt, Phys. Rev. B **74**, 195118 (2006).